Lliso-Ferrando, JR.; Gasch, I.; Martínez-Ibernón, A.; Valcuende Payá, MO. (2022). Effect of macrocell currents on rebar corrosion in reinforced concrete structures exposed to a marine environment. Ocean Engineering. 257:1-12. https://doi.org/10.1016/j.oceaneng.2022.111680

Effect of macrocell currents on rebar corrosion in reinforced concrete structures exposed to a marine environment

J.R. Lliso-Ferrando[a,], I. Gasch[a], A. Martínez-Ibernón[a], M. Valcuende[b]*

[a] Research Institute for Molecular Recognition and Technological Development (IDM), Universitat Politècnica de València, Camino de Vera, s/n., 46022 Valencia, Spain.

[b] Department of Architectural Constructions, School of Architecture, Universitat Politècnica de València, Camino de Vera, s/n., 46022 Valencia, Spain.

**Corresponding author. Tel.: +34 655633238; E-mail address: jollife2@arq.upv.es*
Address: Electrochemistry Laboratory, 1B-ETSIE, Universitat Politècnica de València, Camino de Vera, s/n., 46022 Valencia, Spain

Abstract

Autonomous corrosion monitoring systems in reinforced concrete structures tend to use sensors that are electrically isolated from rebars. This monitoring strategy ignores the macrocell currents that take place between active and passive areas of reinforcement. The effect of these currents has been studied on rebar corrosion in structures exposed to a marine environment. The results showed the existence of macrocell currents generates greater anodic polarisation in rebars' active areas, which favours chloride migration towards steel surface. As a result, corrosion onset takes place sooner, the concentration of the chlorides is higher, and the corrosion rate increases. When a rebar is in passive state, steel mass loss is negligible due to macrocell currents. However, after corrosion onset, the influence of these currents is greater the worse concrete quality is, and the smaller cover is. The corrosion rate showed differences of almost two orders of magnitude in concrete C30 and of one order of magnitude in concrete C50. When the total corrosion rate is determined only by measuring microcell currents, the obtained values tend to underestimate the mass loss due to corrosion by 90%. Conversely, when the analysis includes macrocell currents, a good fit between the theoretical and real values is obtained.

Keywords

Reinforced concrete, corrosion, macrocell current, chlorides, marine environment.

1-. Introduction

The corrosion of rebars embedded in reinforced concrete structures (RCS) is one of the main causes of premature deterioration and failure when they are located in marine environments (Vélez et al., 2011; Qiao et al., 2016; Balestra et al., 2019; Liang and Wang, 2020; Pushpakumara and Thusitha, 2021; Torres-Acosta et al., 2021; Torres-Acosta and Castro-Borges, 2021). This phenomenon reduces their service life and leads to huge economic losses (Moradian et al., 2012).

Rebars are protected by a concrete cover that acts as a physical barrier against aggressive agents (Poursaee, 2016). Thanks to the cementitious matrix's high alkalinity, cover also acts as a chemical barrier because a layer of oxides forms on rebars that reduces ionic mobility and steel dissolution with negligible values (passive film) (Carnot et al., 2003; Bagheri and Rastegar,

2019). These conditions cannot be sustained perpetually when structures are located in marine environments given concrete's permeability: chloride may reach rebars and favour steel depassivation (Montemor et al., 2003). As a result of concrete's heterogeneity, chloride ions do not reach rebars uniformly, but locally, which triggers the appearance of pitting. In these regions, anodic and cathodic areas co-exist (Evans, 1978; Mansfeld, 1971; Bertolini et al., 1996) whose generated current (microcell curent) is added to the current that occurs between the corroded and uncorroded areas (macrocell current) that are electrically connected to one another (Soleimani et al., 2010; Valipour et al., 2014). This means that the real rebar corrosion affected by this phenomenon corresponds to the sum of both current intensities (Qian et al., 2006; Andrade et al., 2008; Andrade, 2019) (Eq. 1) Figure 1.

$$i_{CORR} = i_{CORR,MICRO} + i_{CORR,MACRO} \qquad (Eq.\ 1)$$

In accordance with Faraday's law, this current can also be expressed in corrosion rate terms (V_{CORR}), which is steel section loss by corrosion:

$$V_{CORR}\ (\mu m/year) = 1.17 \cdot i_{CORR}\ (\mu A/cm^2) \qquad (Eq.\ 2)$$

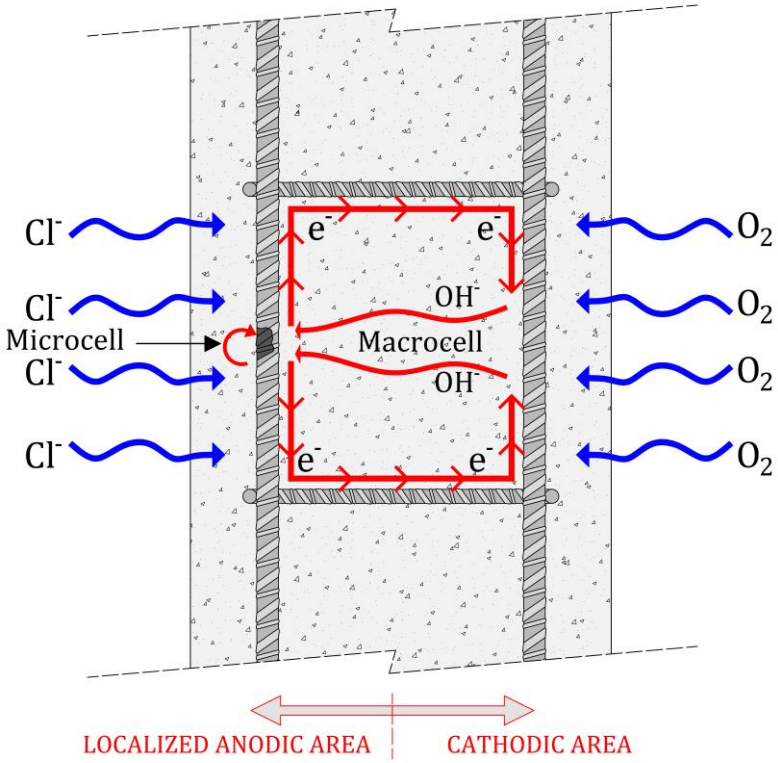

Figure 1- Microcell and macrocell corrosion

The seriousness and cost of the damage caused by corrosion in RCS, and the increasing use of reinforced concrete in harbour and offshore structures (Fernández and Pardob, 2013), have led many researchers to design embedded monitoring systems to determine the corrosion rate without having resort to test boring or *in situ* inspections. Furthermore, these systems are really interesting if we consider that most structures located in marine environments present partial or complete inaccessibility to take on-site corrosion measurements. Furthermore, according to the codes for durability design in many countries, it is compulsory for projects of structures to include an inspection and maintance plan, which makes correct monitoring very important.

In recent years, much progress has been made in developing embedded sensors capable of detecting the depassivation of reinforcement (Andrade, 2020; Daniyal and Akhtar, 2020; Rodrigues et al., 2021), and of measuring the electrochemical potential of adjacent rebars (Karthick et al., 2018; 2019) or the resistivity of concrete cover (Ramón et al., 2021). Other authors have designed sensors to determine the presence of chlorides or concrete carbonation (Gandía-Romero et al., 2016a; 2016b; Ramani and Kuang, 2020), as well as to quantify other corrosion kinetic-related parameters; for example, humidity or oxygen concentration (Martínez-Ibernón et al., 2021). Nonetheless, the most interesting parameter to properly evaluate and control a structure's durability is the corrosion rate because it provides quantitative information about steel section loss owing to corrosion. One of the first examples of this kind of sensors was developed by Martínez and Andrade (2009), in which corrosion rate measurements were taken by the galvanostatic pulse method. Figueira (2017) presented a similar system, which estimated the corrosion rate by the polarisation resistance technique. Another monitoring system was designed by Ramón et al. (2016), who simplified existing models. The measuring technique is set up as a 2-electrode arrangement to avoid resorting to a reference electrode (Martínez-Ibernón et al., 2019; Ramón et al., 2016; 2020). A common characteristic of all the above-cited sensors is that the measurement technique is applied to the working electrode electrically isolated from rebars while corrosion is being measured. Therefore, sensors do not measure the macrocell current, and only local corrosion is recorded (microcell current).

Not many research works have analysed the importance of macrocell currents on rebar corrosion. Most have focused on solution studies (Andrade et al., 1992, 2008; Dong and Poursaee, 2020, Chen and Su, 2021), but the obtained results are not representative of the situation that actually occurs in RCSs (Lliso-Ferrando, 2021). The few conducted studies about concrete have obtained very different results. For instance, Valipour et al. (2014) pointed out that macrocell currents are only a small part of the corrosion rate (5-10%), while François (2022) considered that these currents correspond to about 100% total corrosion. Other studies indicate that macrocell currents represent about 30% total corrosion (Hansson et al., 2006; Subramaniam et al., 2010). Revert et al. (2019) obtained values between 20% and 55%, while Rodríguez et al. (1999) reported values of 70%. These different results in the bibliography are also conditioned by the testing conditions under which these studies were performed.

As the uncertainties about the importance of macrocell currents in RCSs' corrosion processes are substantial, it is necessary to analyse this aspect because autonomous monitoring systems do not take them into account. To correctly quantify rebar corrosion rates, that is, their section loss due to corrosion, it is essential to ensure the structure's security, evaluate its service life and avoid costly repair processes. Consequently, the objective of this research work was to study both the influence of macrocells on rebar corrosion and the importance of contemplating them in corrosion monitoring systems for RCS exposed to a marine environment. To do so, rebars were embedded in concretes with different compressive strengths and distinct covers. Specimens were partially submerged in 3% NaCl solution for almost 1 year and the corrosion rate of the embedded rebars was monitored. Research was conducted using a large cathodic surface that simulates the conditions that would take place in densely reinforced areas like those in marine structures. A gravimetric comparison between the mass loss estimated according to the corrosion monitoring results and real mass loss was made for the study validation. Chloride diffusion inside the material was also studied to estimate the time that chlorides take to reach rebar surface.

2-. Experimental plan

2.1.-Materials

In order to manufacture the specimens herein used, four concrete types with different characteristics and properties were prepared: low-strength concrete 30 MPa (C30); high-strength concrete 50 MPa (C50); very high-strength concrete (C90); ultra high-performance fibre-reinforced concrete (UHPFRC, UH-150). The characteristics of each mix appear in Table 1. All the concretes were made using CEM I 42.5 R/SR. For concretes C90 and UH-150, silica fume (Elkem Microsilica®) was also included in the mix. For concrete type UH-150, siliceous flour with a similar particle size distribution to the cement and steel fibres in 2%(vol.) (Ø0.2 mm; 13 mm) was used. All the specimens were cured at 20±2ºC and 95% relative humidity (RH) until the age of 28 days.

Table 1- Mixture proportions of concretes (kg/m^3)

	C30	C50	C90	UH-150
Cement	292	450	500	800
Water	190	225	178	160
Superplasticizer Sika®-20HE	2.80	1.37	3.50	30
Silica fume			55	175
Siliceous flour				225
Siliceous sand fine (0/0.5)				302
Siliceous sand medium (0.6/1.2)				565
Limestone sand (0/4)	1256	880	914	
Limestone gravel (4/8)		880	779	
Limestone gravel (4/12)	707			
Steel fibres (Ø0.2mmx13mm)				175
w/c ratio	0.65	0.50	0.36	0.20
w/b ratio	0.65	0.50	0.32	0.16
f_c (28 days) (MPa)	30.67	49.88	88.86	135.43

2.2.-Test methods

In order to know resistance to chloride diffusion, the diffusion coefficient was analysed in the non-stationary state for each concrete type. At the same time, the corrosion on the embedded rebars was followed up. The compressive strength at the age of 28 days was determined from each mix on cylindrical specimens (Ø = 100 mm; height = 200 mm) (Table 1).

2.2.1.- Chloride diffusion test

Chlorides penetrate through the cementitious matrix mainly by diffusion (De Medeiros-Junior et al., 2015; Balestra et al., 2020). The unidirectional diffusion coefficient of each concrete type was obtained according to European Standard EN 12390-11 (AENOR, 2019). Testing was done with cylindrical samples (Ø = 100 mm; height = 100 mm) exposed to a unidirectional chloride diffusion flow. For this purpose, a water tank (300 mm high) with 3% NaCl solution was placed on one of the specimen sides and epoxy coating was applied to the others, as described in the standard method (AENOR, 2019). Specimens were left under these conditions for 90 days. After this period, the chloride concentration was measured at different depths. The chloride content of each sample was obtained as set out in Standard NT Build 208 (NORDTEST, 1996). For concrete UH-150, the steel fibres in each sample were removed by an electromagnet

before running the chloride content analysis. Testing was done on three samples for each concrete type and the result for each mixture was taken as the arithmetic mean of the three recorded values.

2.2.2.- Corrosion monitoring

The monitoring of macrocell and microcell corrosion ($i_{CORR,MACRO}$ and $i_{CORR,MICRO}$) was done on cubic specimens (150x150x150 mm^3) with three embedded rebars (Ø10 = mm; 150 mm long), as described in Figure 2.

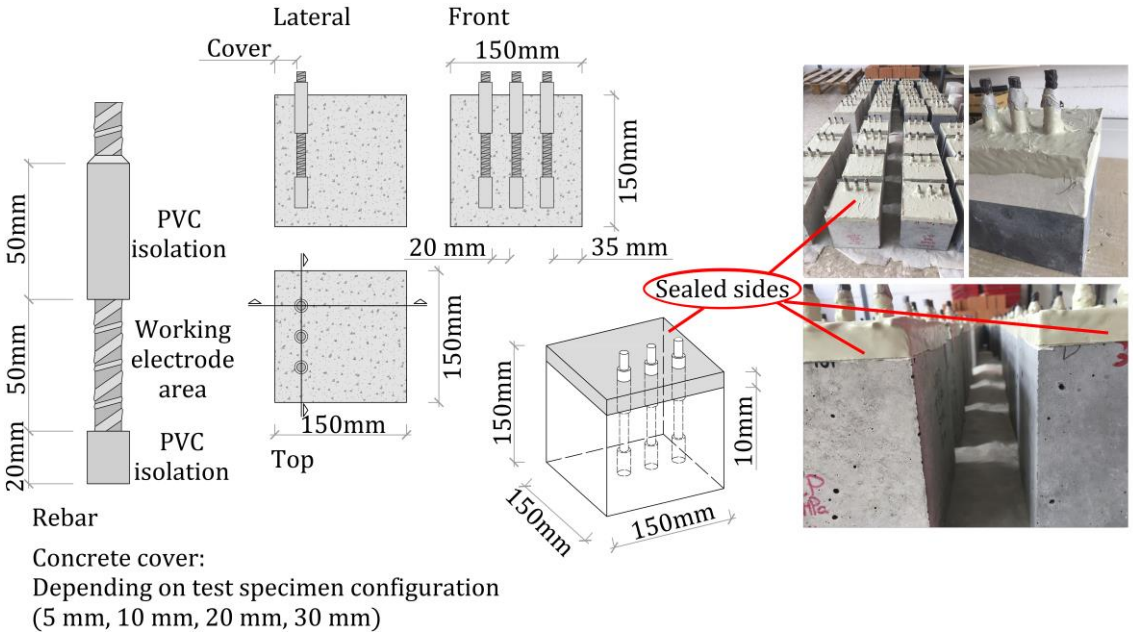

Figure 2- Test specimens' configuration

Rebars were partly covered by epoxy and a PVC pipe (Figure 2) to delimit the surface that came into contact with concrete (working area) at 15.71 cm^2, and were arranged on the specimen with different covers: 5 mm, 10 mm, 20 mm and 30 mm. Two specimens for each concrete type and cover were made. After a curing period in a humid chamber, the upper side was sealed with epoxy coating. Then specimens were partly immersed in 3% NaCl solution and were left under these conditions for almost 1 year.

Along with each specimen, a carbon fibre meshing piece was placed (600 cm^2 surface area). This piece was electrically connected to the two lateral rebars (Figure 3). The rebars in each specimen were divided into two groups: two rebars connected (C) to the carbon fibre meshing piece and one was not connected (NC). Using carbon fibre mesh as a cathode allows the oxygen present in solution to be adsorbed on its surface and to undergo a reduction process with the electrons from rebars to simulate rebar behaviour in the passive state. Another advantage of using carbon fibre mesh is that no oxidising takes place under dissolution conditions. In this way, a macrocell current was established between rebars (active area) and mesh (passive area).

For each concrete type and cover, the microcell current of two rebars (NC rebars) was monitored, as were the macrocell and total currents in four other rebars (C rebars). In all, 96 rebars were monitored. Table 2 lists the number of rebars and the nomenclature used in this work.

Table 2- Rebars, configuration and nomenclature of specimens.

Concrete type	C30		C50		C90		UH-150	
Electric configuration	**(C)**	**(NC)**	**(C)**	**(NC)**	**(C)**	**(NC)**	**(C)**	**(NC)**
Cover: 5 mm (+5)	4	2	4	2	4	2	4	2
Cover: 10 mm (+10)	4	2	4	2	4	2	4	2
Cover: 20 mm (+20)	4	2	4	2	4	2	4	2
Cover: 30 mm (+30)	4	2	4	2	4	2	4	2
Total rebars	**96 rebars**							

(C-Connected and NC-Not Connected to carbon fibre mesh)

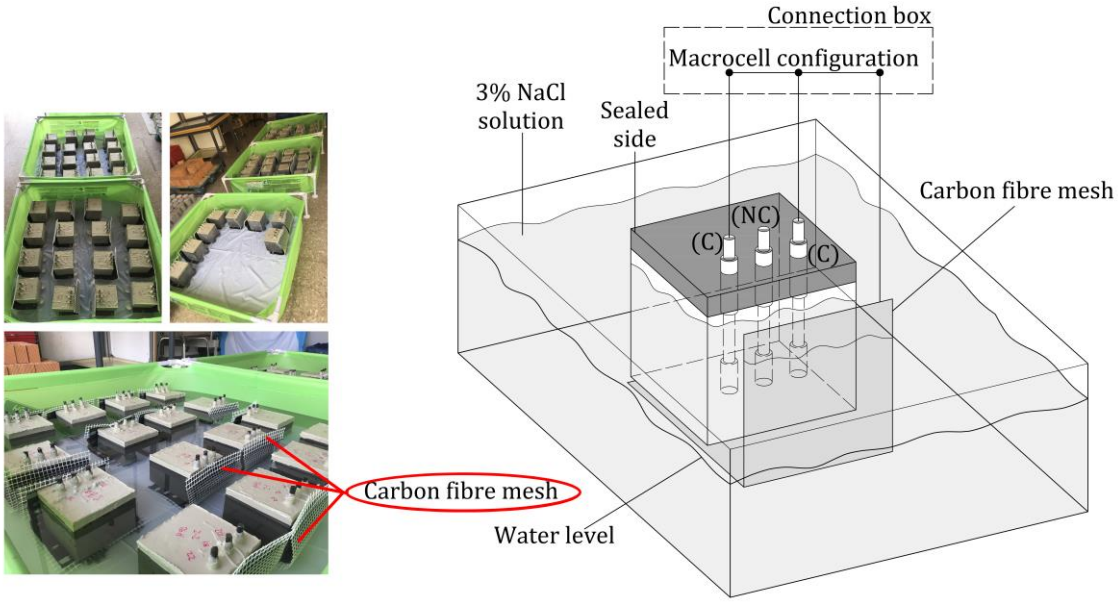

Figure 3- Electrical configuration

When rebars C were connected to carbon fibre mesh, the net current flow between it and the two rebars of each specimen was measured by a Zero Resistance Ammeter (ZRA; Keithley 2000 Tektronix model). The value obtained for each rebar was normalised by its surface (15.71 cm^2). This current corresponds to the macrocell current ($i_{CORR,MACRO}$). The value was recorded 1 minute after measurements commenced to ensure that the recorded signal was stable enough (Figure 4).

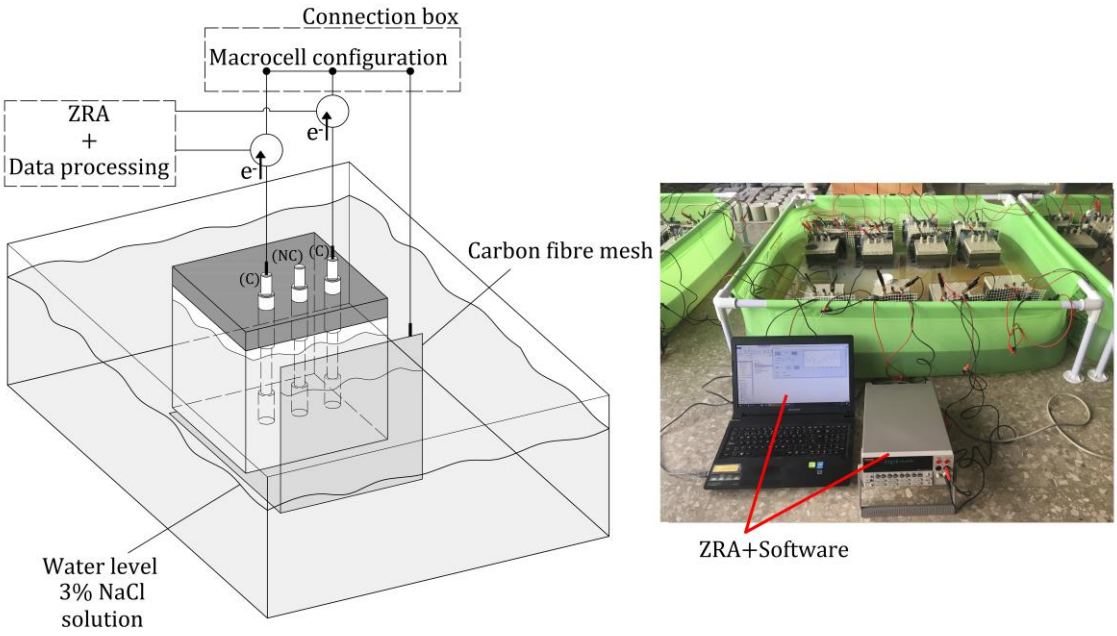

Figure 4- Macrocell measurement configuration

Moreover, rebar corrosion current density ($i_{CORR,MICRO}$) was periodically measured in all the rebars (C and NC) by the potentiostatic step voltammetry (PSV) technique described in (Martínez-Ibernón et al., 2019; Ramón et al., 2019, 2020). This measurement system allows rebar corrosion to be analysed by studying the response of steel to potentiostatic-type disturbance. The measurement was taken with an Autolab PGSTAT 100 Potentiostat. The measuring cell arrangement was a 3-electrode one: the working electrode on which corrosion was measured was each rebar; the reference electrode was a saturated calomel electrode (SCE) partly immersed in solution; the carbon fibre mesh of each analysed specimen was used as the counter electrode. The obtained result was also normalised by the rebar surface (15.71 cm^2) to obtain microcell current intensity ($i_{CORR,MICRO}$). To take this measurement, bars must be electrically disconnected from carbon fibre mesh. After taking measurements, rebars (C) were reconnected to mesh to continue participating in macrocell processes until the next measurement was taken.

During the monitoring period, the water level was always 1.5 cm below the upper specimen side thanks to a level sensor being used. Every 2 weeks, the chloride content in solution was controlled to ensure that the chloride concentration remained constant. To do so, water samples were taken and analysed by Mohr's method (Standard UNE-ISO 9297:2013) (2013).

Specimens were subjected to rebar inspection at the end of the corrosion monitoring period. For this purpose, rebars were removed from specimens and cleaned for a 10-minute cycle in $0.1M\ H_3PO_4$, which was repeated twice. Afterwards, a gravimetric comparison between the estimated mass loss was made according to the corrosion monitoring results and the real mass loss.

3.- Results and Discussion

3.1.- Chloride diffusion test

Figure 5 shows the chloride content (% per cement weight) obtained for each analysed sample in relation to the depth at which samples were taken.

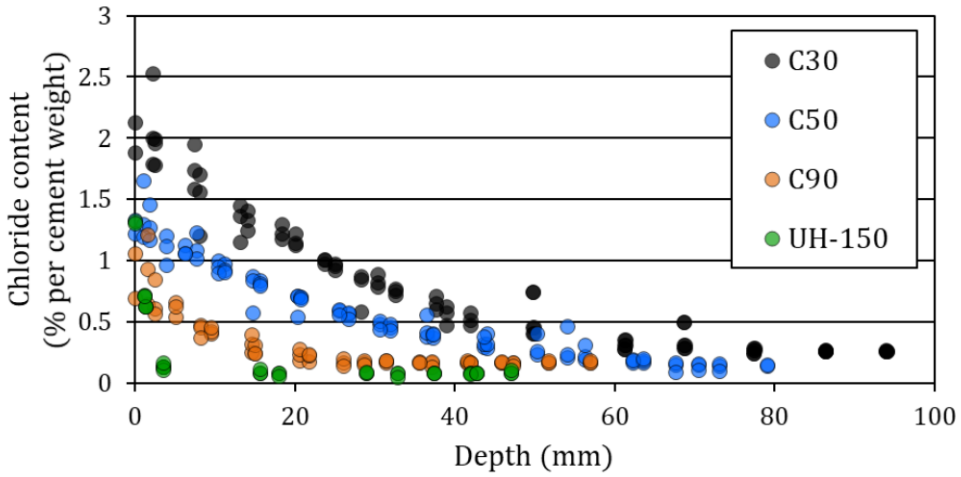

Figure 5- Chloride content per cement weight (%) depending on depth

With these data, and in line with European Standard EN 12390-11 (AENOR, 2019), the D_{app} coefficient value was calculated by Fick's second law, Eq. 3:

$$C(x,t) = C_0 + (C_s - C_0) \cdot \left[1 - \operatorname{erf}\left(\frac{x}{2\sqrt{D_{app} \cdot t}}\right)\right] \qquad (Eq.\ 3)$$

where D_{app} is the non-steady state diffusion coefficient, expressed as m^2/s, C_s is the chloride concentration on the concrete surface, C_0 is the initial chloride concentration (chloride content in % mass prior to immersion in NaCl solution) and $C(x,t)$ is chloride content in the % of cement weight obtained at a given depth (x) and for a given exposure time (t). The initial chloride content (chloride contributed by raw materials) was obtained from the samples not contaminated by chloride solution, with 0.03% in UH-150, 0.04% in C90, and 0.09% in C30 and C50. The surface chloride concentration (C_s) and the D_{app} coefficient were obtained by fitting Eq. 3 to the experimental data on the chloride concentration at different depths (Figure 5) by a non-linear least squares' regression analysis. Figure 6 shows the curve fitting with the experimental data obtained for each concrete type.

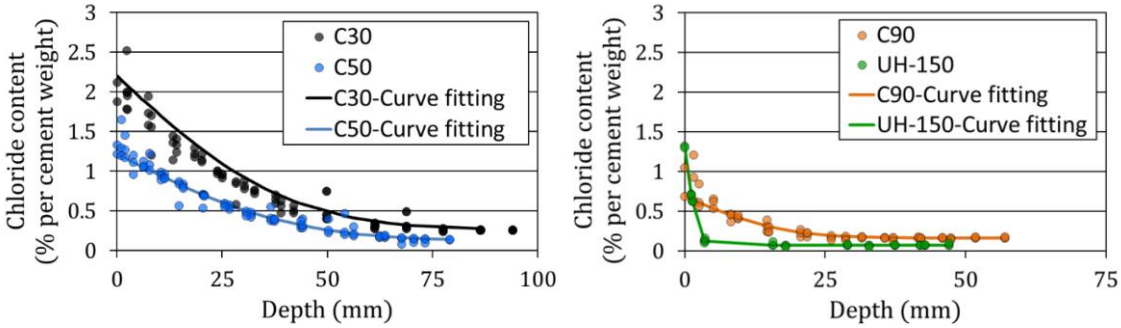

Figure 6- Experimental values and curve fitting depending on the concrete type

Table 3- D_{app} results

	C30	C50	C90	UH-150
D_{app} (x10^{-11} m/s^2)	6.806	4.326	0.111	0.031

Table 3 shows the average D_{app} coefficient value obtained for each concrete type. This parameter is a good indirect indicator of materials' durability because it represents resistance that materials confer chloride diffusion. The results demonstrated a huge difference between the different concretes. Concrete UH-150 had the lowest value thanks to a very dense microstructure, as previous works have shown (Valcuende et al., 2021a; 2021b). The D_{app} value obtained with concrete C90 was one order of magnitude higher than that for UH-150. Using higher size aggregates increased the heterogeneity of porous structure, which facilitated greater chloride diffusion. The mixture of both concretes C90 and UH-150 included silica fume, which segmented the capillary network and favoured tortuosity (Dotto et al., 2004; Kupwade-Patil et al., 2018; Bentz et al., 2000). This characteristic distinguished these concretes from C30 and C50 by having a much higher D_{app} value (about two orders of magnitude higher than UH-150).

The interest in this value lies in the possibility of estimating the required period of time for chlorides to reach rebars and corrosion onset. This time is calculated by Eq. 4, which was obtained from Eq. 3:

$$t = \frac{x^2}{4 \cdot D_{app} \cdot \left[erf^{-1}\left(\frac{C_s - C_{crit}}{C_s - C_0}\right)\right]^2} \qquad (Eq.\ 4)$$

where erf^{-1} is the inverse Gaussian error function, x is the rebar cover depth, and C_{crit} is the critical chloride concentration threshold that alters rebar passive layer stability and leads to corrosion onset. The C_{crit} parameter is not a well-defined value in the scientific literature. The higher the chloride concentration on the steel surface, the more likely corrosion onset is. A wide range of values has been suggested (Angst et al., 2009; Angst, 2011, 2019; Gao et al., 2019). By taking the 0.6% cement weight as a value that some recommendations propose (Ministerio de Fomento, 2008), Figure 7 represents the corrosion onset curves according to concrete cover.

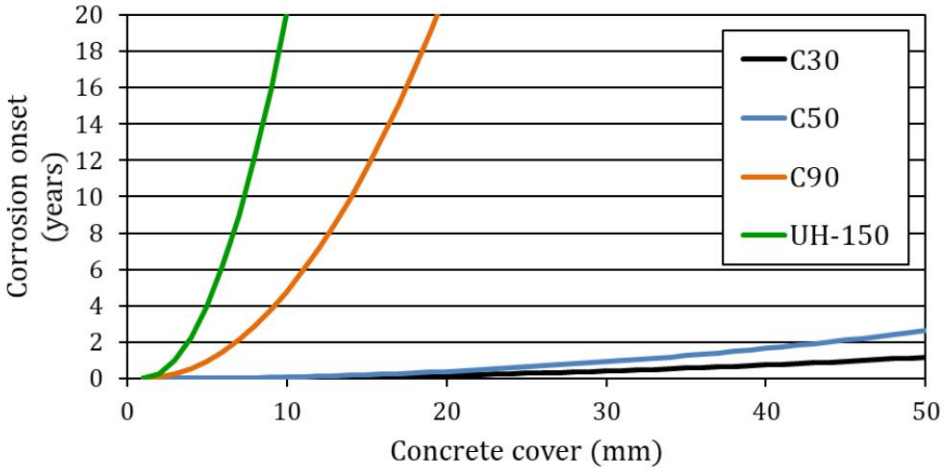

Figure 7- Corrosion onset depending on concrete type and concrete cover

According to Figure 7, it is possible to calculate the time needed for corrosion onset for the concrete types and covers used in the specimens described in Section 2.2.2. Table 4 offers the calculated values. These are approximate values and cannot be taken as certain values. However, they allow comparisons to be made between different concretes.

Table 4- Time period (years) estimated for rebar depassivation according to concrete type and cover

	C30	C50	C90	UH-150
Cover: 5 mm (+5)	0.01	0.03	1.08	5.62
Cover: 10 mm (+10)	0.05	0.12	4.32	22.47
Cover: 20 mm (+20)	0.20	0.47	17.26	89.89
Cover: 30 mm (+30)	0.44	1.05	38.83	202.36

3.2.- Microcell corrosion current ($i_{CORR,MICRO}$)

Figure 8 depicts the average microcell corrosion current value ($i_{CORR,MICRO}$) of the rebars embedded in specimens. In each graph of Figure 8, the limit value is marked at 0.1 µA/cm^2, which is the threshold indicated by the Rilem TC-154 EMC recommendation (2004) below which the corrosion rate can be considered negligible. This document also points out that the 0.1-0.2 µA/cm^2 range of values can be taken as a transition zone between the passive and active corrosion states. The graphics also point out the threshold of 1 µA/cm^2, which is the limit from which the corrosion rate is high.

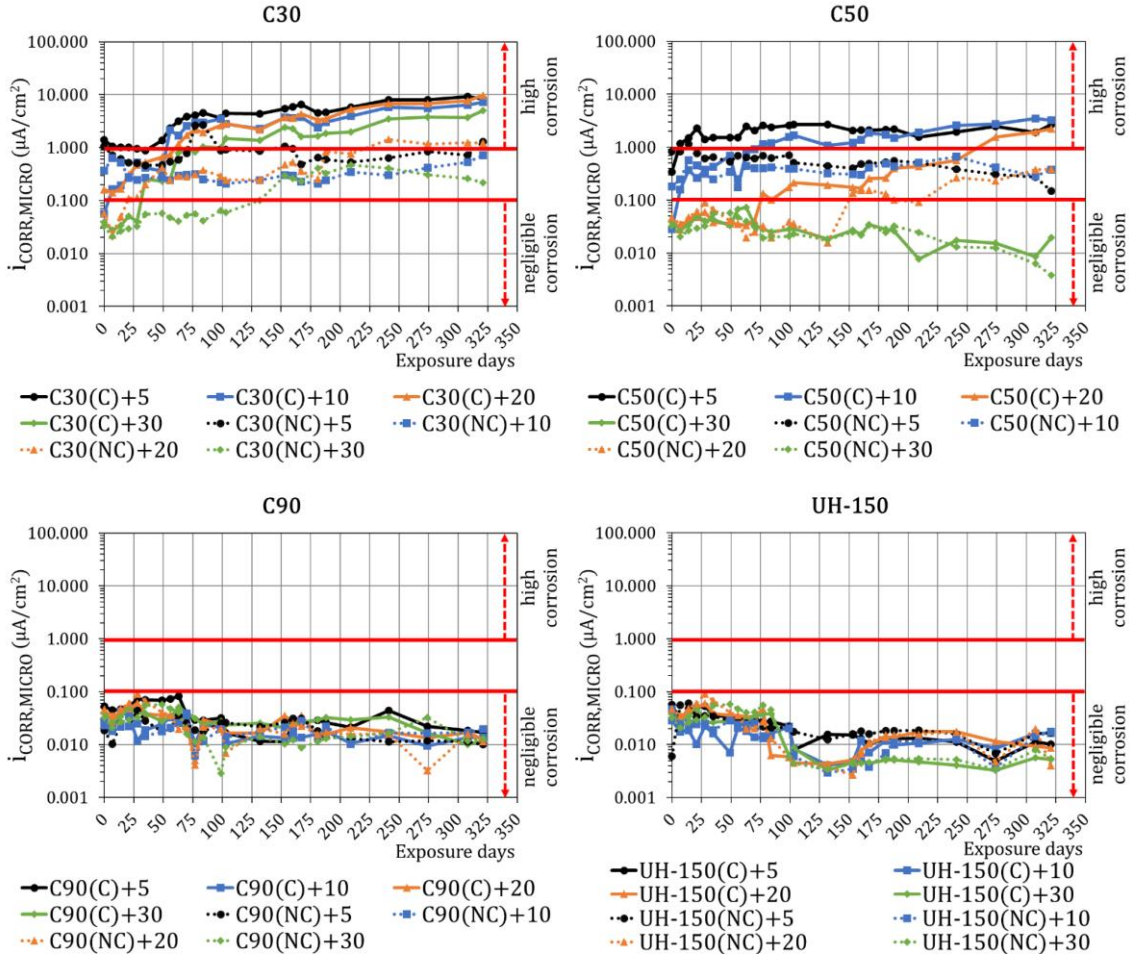

Figure 8- Microcell corrosion current depending on concrete type and concrete cover

3.2.1. Effect of concrete type and concrete cover

Corrosion started in all the rebars embedded in the C30 specimens. The $i_{CORR,MICRO}$ values over 0.1 µA/cm^2 were recorded on the first days for the rebars with less cover (5 mm). The

time needed for the bars with a bigger cover to undergo these increases was longer and closely related to the data obtained in Table 4. Thus, for example, for the rebars with the 30 mm cover, depassivation was estimated to take place at the age of 0.44 years (160 days), which coincides with the age at which the NC rebars actually started to present values above 0.1-0.2 µA/cm^2 (≈151 days).

This same trend was noted in specimens C50. With the 20 mm cover, the corrosion levels of the rebars with the NC configuration exceeded 0.1 µA/cm^2 after about 150 days. This result matches the estimation of 0.47 years (≃ 170 days) set by the calculations done with the obtained D_{app} (Table 4). For the specimens C50 with a 30 mm cover, the $i_{CORR,MICRO}$ values were below 0.1 µA/cm^2, which indicates that rebars had still not depassivated. The forecasted time before the surface of these rebars reached the critical chloride content took longer than 1 year (≃ 390 days) (Table 4). This information agrees with the fact that no corrosion signs were detected after the 320-day follow-up (see Section 3.5).

The very high resistance of concretes C90 and UH-150 to chloride diffusion, as shown by the diffusion test and the estimated data found in Table 4, as well as their high electrical resistivity (Valcuende et al., 2021a), justify that no corrosion was recorded in these concretes (Figure 8). All the rebars had values below 0.1 µA/cm^2. For the most unfavourable case (5 mm cover), the corrosion current at the end of the monitoring period was 0.028 µA/cm^2 in concrete C90 and 0.015 µA/cm^2 in concrete UH-150.

3.2.2. Effect of connection between rebars and carbon fibre mesh on microcell corrosion currents

As observed in the graphs of Figure 8, especially for concretes C30 and C50, the rebars that were connected to carbon fibre mesh (C rebars) (to simulate the connection to other passive reinforcements) tended to depassivate at earlier ages and reached higher corrosion rates than the isolated rebars (NC rebars). Thus, for example, with specimens C30 and a 30 mm cover, the corrosion onset in the NC rebars occurred at 151 days, while the corrosion onset in the C rebars took place at 30 days. Furthermore, the $i_{CORR,MICRO}$ reached a value of 0.38 µA/cm^2 in the NC rebars and 5.1 µA/cm^2 in the C rebars, which is more than one order of magnitude difference between them. This tend was also observed in concrete C50 for covers up to 20 mm.

What these data reveal is that a connection to passive reinforcements accelerates corrosion onset and increases microcell corrosion kinetics. This is because chloride ions (negative electrical charge) are attracted by steel, which has a positive electrical charge as a result of the current flow between the rebar and carbon fibre mesh. Thus, when a macrocell current is present (as in the C rebars), chloride diffusion is intensified by a migration process. This fact was demonstrated by the total chlorides analysis performed in the surroundings of the C and NC rebars embedded in several specimens (Figure 9) at the end of the follow-up period. The chloride content around the rebars subjected to macrocell currents (connected rebars) was between 80% and 600% higher than in the NC rebars.

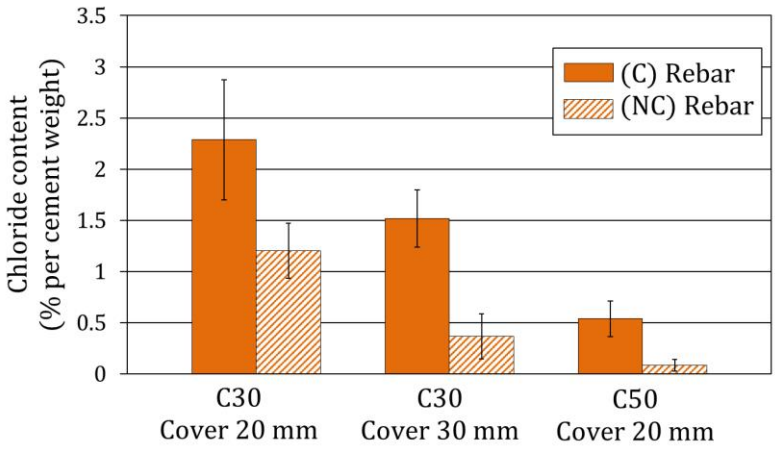

307

308 *Figure 9- Chloride content (% per cement weight) around rebars*

309 ## *3.3.- Macrocell corrosion current ($i_{CORR,MACRO}$)*

310 Figure 10 depicts the average macrocell corrosion current value ($i_{CORR,MACRO}$) of the rebars
311 connected (C) to carbon fibre mesh.

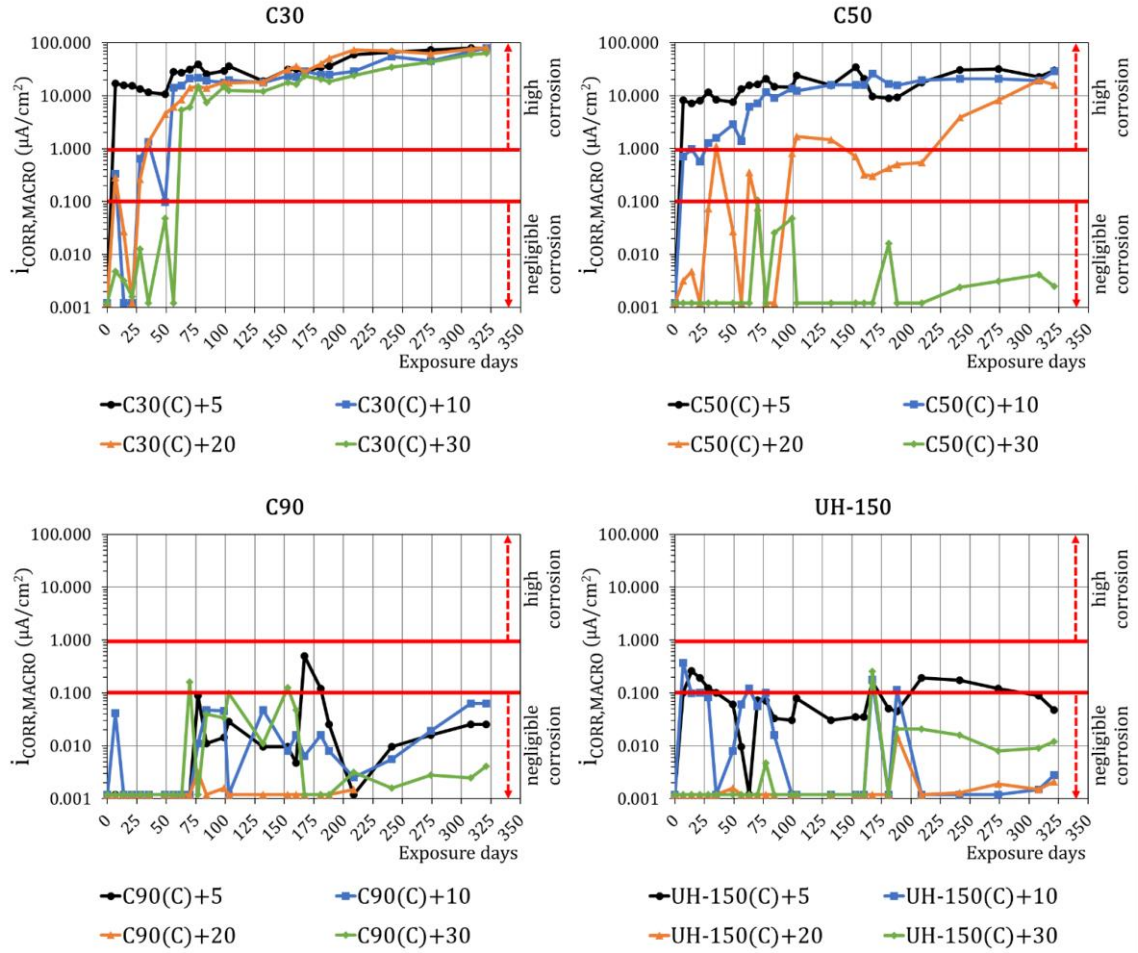

312

313 *Figure 10- Macrocell corrosion current depending on concrete type and concrete cover configuration*

314 The macrocell current evolution displayed a similar trend to corrosion $i_{CORR,MICRO}$. Significant
315 increases in $i_{CORR,MACRO}$ took place on the first days for the rebars embedded in concrete C30
316 (at 10 days in the rebars with a 5 mm cover, at 30 days in the rebars with covers of 10 mm and

20 mm, and at 60 days for the rebars with a 30 mm cover). In fact, the $i_{CORR,MACRO}$ values were higher than 10 µA/cm^2 in all cases, which denotes very high corrosion levels. This behaviour was also noted for the rebars embedded in concrete C50 for the 5 mm and 10 mm covers. This trend was repeated for the rebars with a 20 mm cover whose values were 1 µA/cm^2 after 225 days.

In concretes C90 and UH-150, macrocell current intensity was below 0.1 µA/cm^2 throughout the study period. These concretes' high resistance to chloride diffusion (Section 3.1.) hindered chloride ions reaching rebars during their exposure period. Moreover, limited permeability to gas (Valcuende et al., 2021a; 2021b) prevents oxygen availability at rebars' depths, which does not allow the onset of corrosion processes. The high electrical resistivity of both these concrete types (Valcuende et al., 2021a; 2021b) also limits ionic mobility, which lowers the possibility of electrochemical processes like corrosion taking place.

3.4.- Total corrosion current (i_{CORR}) and mass loss

In order to properly know the rebar corrosion state and the influence of macrocell processes, it is necessary to jointly consider macrocell and microcell corrosions (Eq. 1) to calculate the corrosion current (Figure 11).

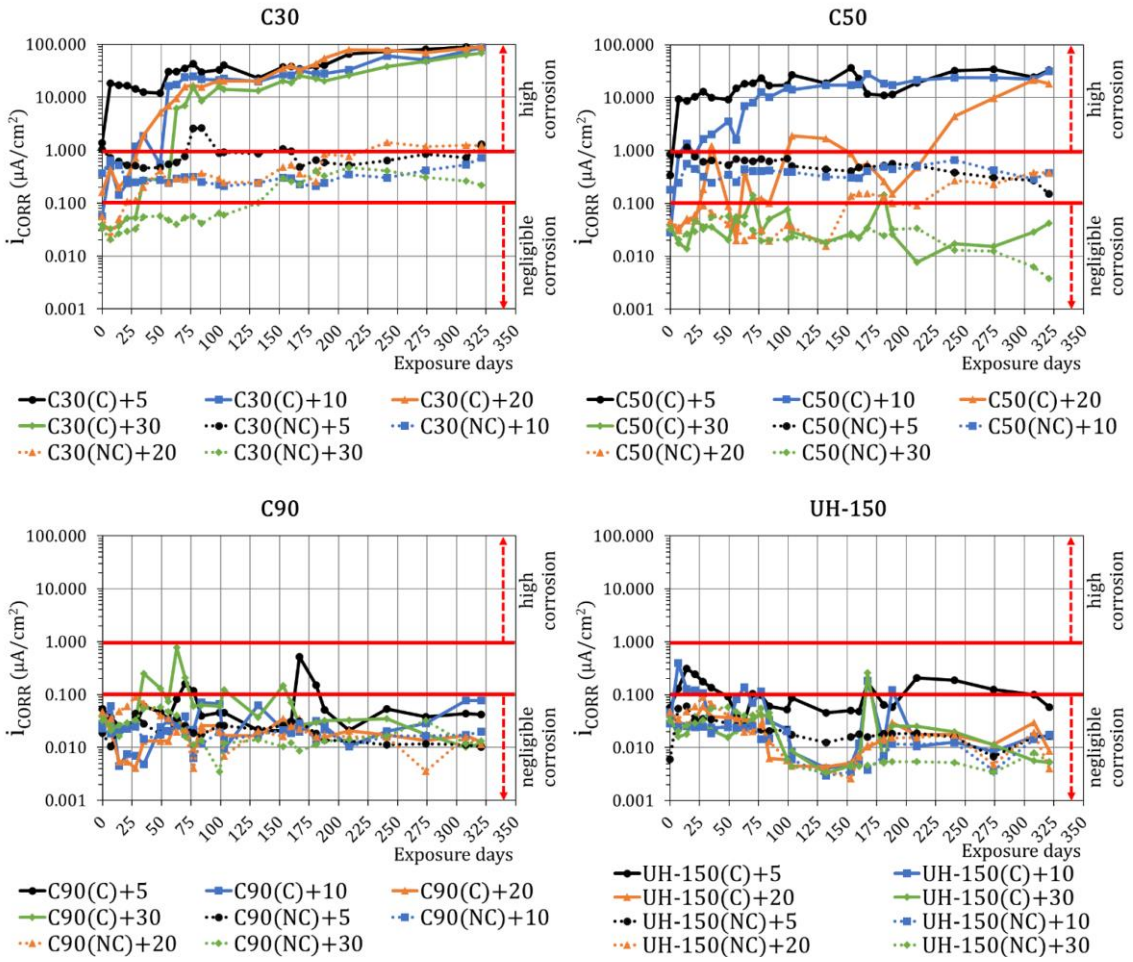

Figure 11- Corrosion current depending on concrete type and concrete cover configuration

In the rebars where corrosion onset was clear (concretes C30, and C50 with 5, 10 and 20 mm covers), a large difference was observed between the rebars that had undergone macrocell processes (C rebars) and those that had undergone only local corrosion processes (NC rebars).

The i_{CORR} values showed differences of almost two orders of magnitude in concrete type C30 and of one order of magnitude in concrete type C50.

The results obtained in concretes C90 and UH-150 were below 0.15 µA/cm^2, even with a 5 mm cover. These data indicate that the repercussion of macrocell currents on the rebars in passive state was minimum.

By integrating the corrosion intensity-time curve, the mass loss ($\Delta m, calc$) that accumulated during the exposure period was calculated in accordance with Faraday's law (Eq. 5), as shown by:

$$\Delta m, calc = \frac{M}{n\,F} \cdot \int_{t_0}^{t} i_{CORR} \cdot dt \qquad (Eq.\ 5)$$

where M is the steel atomic mass (55.845 g/mol), t is the time in seconds, n is the number of electrons released or acquired during the corrosion process (2 for this case) and F is Faraday's constant (96845 C/mol). Mass loss ($\Delta m, calc$) was obtained in g/cm^2 and normalised by rebars' working area (15.71 cm^2).

The obtained results are presented in Figure 12 and Table 5. Figures 12(a) and 12(b) show mass loss after 320 days under the seawater exposure conditions for NC (not connected to macrocell) and C (participating in macrocell processes), respectively. By comparing both graphics, once again mass loss was higher in those specimens that participated in macrocell processes (C). Thus, for example, the average mass loss obtained for C30 (5 mm cover) was 130 mg in specimens NC and was 6600 mg in specimens C; that is, 50-fold more. The data also showed that the influence of macrocell currents was greater the lower the concrete quality was, and the smaller concrete cover was.

It is also noteworthy that mass loss was insignificant due to macrocell currents when a rebar was not depassivated; e.g. for UH-150 (30 mm cover), mass loss was 1.92 mg and 2.81 mg in specimens NC and C, respectively.

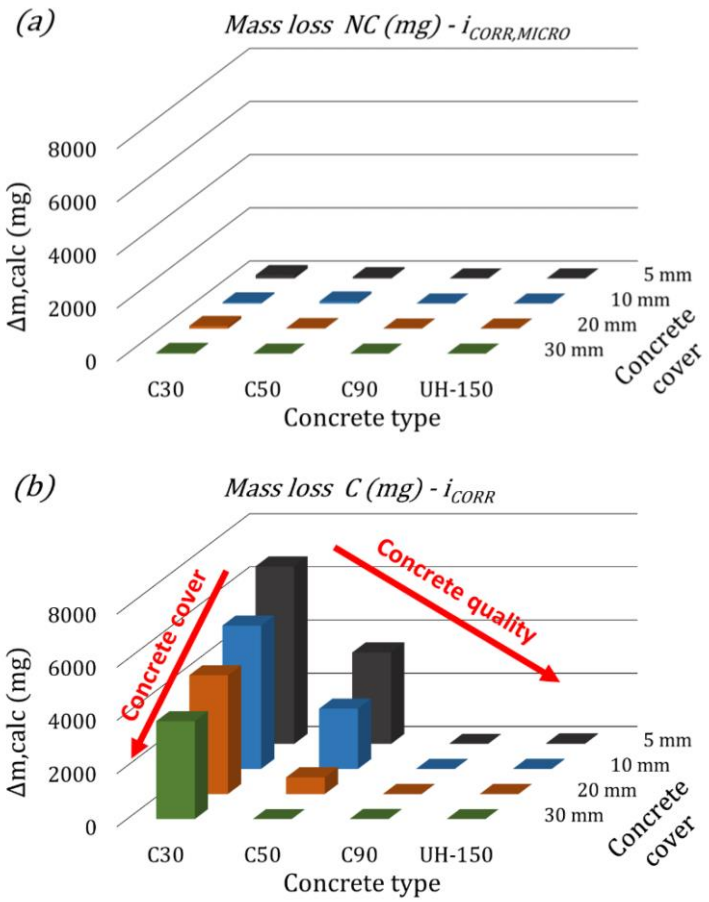

361

362 *Figure 12- Mass loss of rebars considering (a) only corrosion per microcell and (b) total corrosion*

363 *Table 5- Accumulated mass loss (mg)*

Concrete type	**C30**		**C50**		**C90**		**UH-150**	
Electric configuration	**(C)**	**(NC)**	**(C)**	**(NC)**	**(C)**	**(NC)**	**(C)**	**(NC)**
Cover: 5 mm (+5)	6,676.9 (9.58)	128.98 (7.29)	3,442.6 (11.13)	52.57 (13.96)	22.23 (3.97)	2.24 (3.31)	7.09 (2.61)	1.96 (1.68)
Cover: 10 mm (+10)	5,393.7 (13.78)	80.05 (10.40)	2,269.9 (9.15)	45.54 (4.58)	5.91 (1.98)	2.17 (1.12)	4.58 (2.62)	1.75 (1.18)
Cover: 20 mm (+20)	4,468.1 (12.23)	101.12 (5.41)	627.02 (6.91)	21.25 (7.05)	2.30 (2.72)	2.94 (2.94)	3.10 (2.37)	2.62 (1.65)
Cover: 30 mm (+30)	3,679.9 (9.67)	28.64 (2.48)	9.62 (4.13)	2.45 (2.14)	4.03 (2.18)	2.29 (1.81)	1.10 (3.44)	2.02 (1.84)

364 *Numbers in brackets are the coefficients of variation*

365 ## *3.5.- Visual inspection*

366 In order to confirm the obtained results, all the concrete specimens were visually inspected
367 (Figure 13).

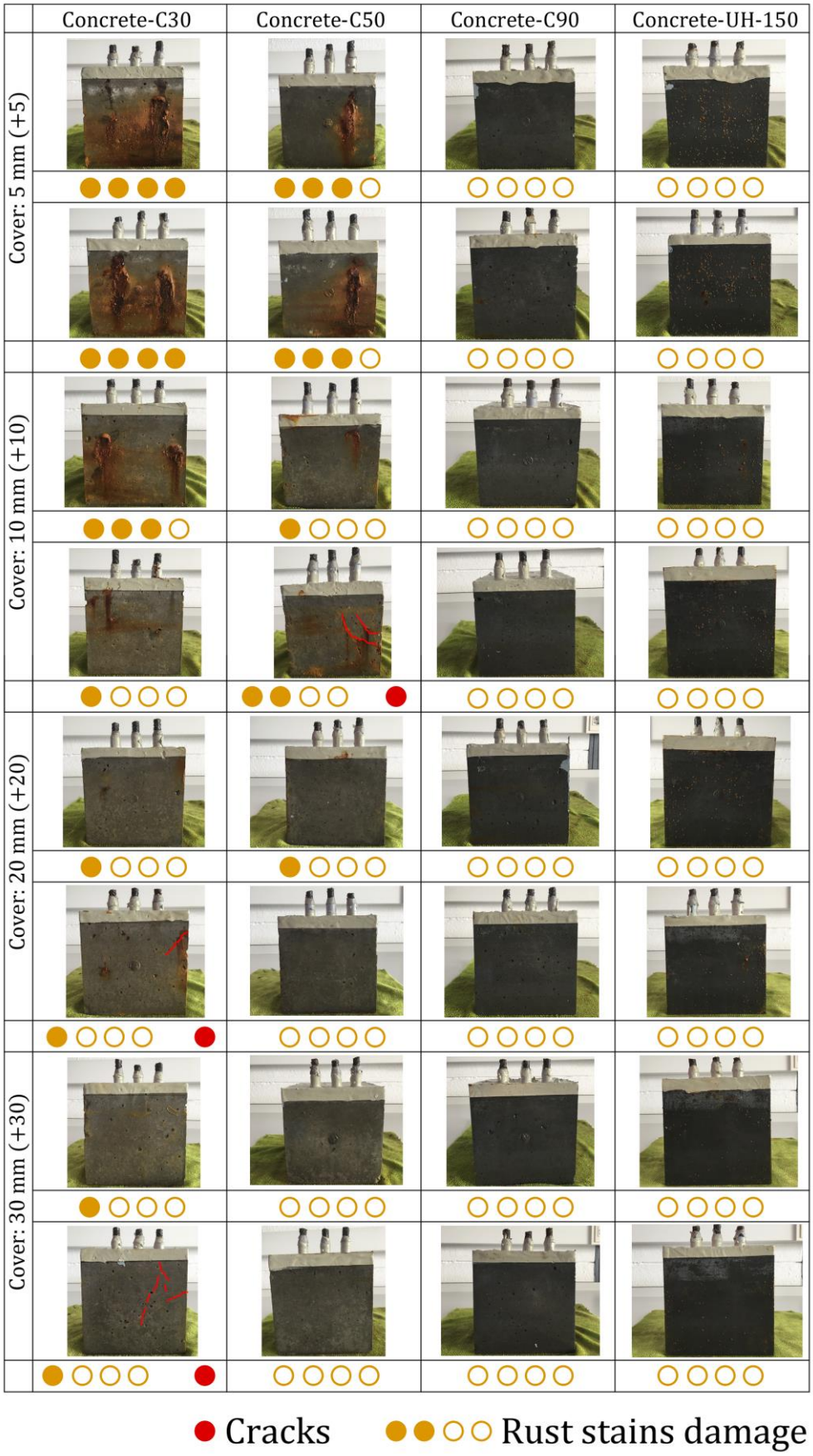

368

369 *Figure 13- The state that specimens were in after being immersed in 0.5M NaCl solution for more than*
370 *320 days*

The damage noted on concretes C30 and C50 was sometimes relevant. For covers 5 mm and 10 mm, specimens presented large rust stains, or even cracking. This damage concentrated on lateral bars; that is, on those connected to carbon fibre mesh (C bars) and, therefore, on those that participated in macrocell processes. For bigger covers (20 mm or 30 mm), much less damage was observed on concrete C30 and damage was almost inexistent on the concrete C50 specimens, which showed only small rust stains and very few small cracks. All these results correspond well to the corrosion rates recorded on these bars (Figure 11).

The visual inspection revealed no damage on specimens C90, and microscopic rust stains on the surface of the UH-150 specimens owing to the corrosion of more superficial steel fibres. Thus oxidation affected only fibres closer to the surface and not inner fibres or rebars (Figure 14).

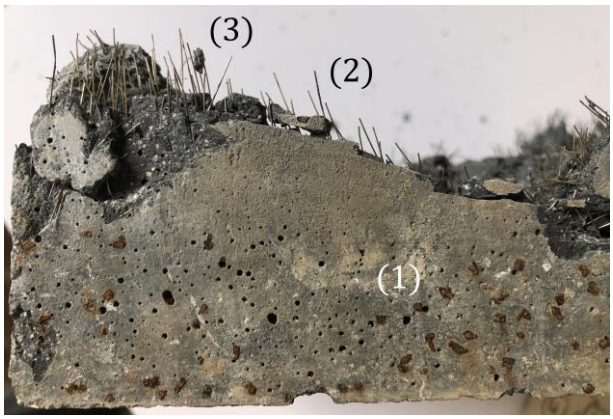

Figure 14- Details of: (1) superficial fibre corrosion; (2) rusty superficial fibres; (3) inner fibres with no corrosion signs

Finally, a visual inspection of rebars was made after removing them from the test specimens. This examination confirmed the strong influence of macrocell processes on total rebar corrosion (Figure 15). For instance, with concrete C30 and 5 mm or 10 mm covers, the rebars that participated in macrocell processes (C rebars) displayed very severe corrosion attack, with marked section loss. This means that the large electrons demanded by carbon fibre mesh brought about greater steel oxidation. Conversely, the rebars that were not electrically connected to mesh (NC rebars) did not display appreciable damage. For bigger covers or other better-quality concretes, this effect was not visually noticeable because the corrosion that occurred during the testing period was very slight or even negligible in many cases.

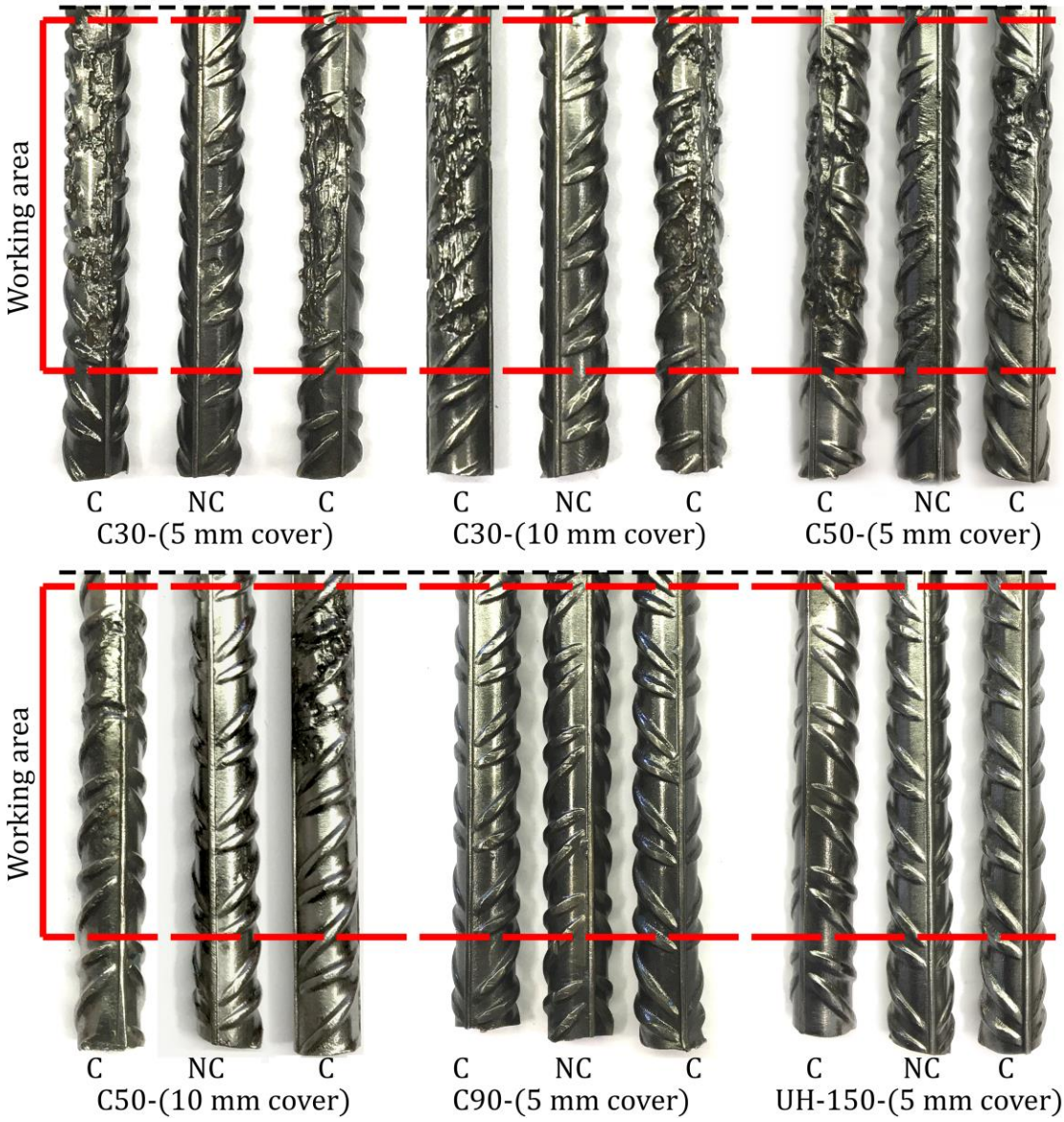

Figure 15- State that the different rebars were in

3.6.- Gravimetric analysis

The gravimetric test is the reference for the correct calibration of the corrosion rate measurement following the RILEM Recommendation of TC 154-EMC (2005). After being exposed to a marine environment for more than 320 days, the rebars that had been weighed before specimens were manufactured were weighed again. In Figure 16 the real mass loss of rebars is represented (gravimetric test) vs. the theoretical loss obtained by Eq. (5) in the two following cases: a) considering only microcell processes ($i_{CORR,MICRO}$); b) considering the total corrosion current *(i_{CORR})* obtained from the sum of ($i_{CORR,MICRO}$) and ($i_{CORR,MACRO}$).

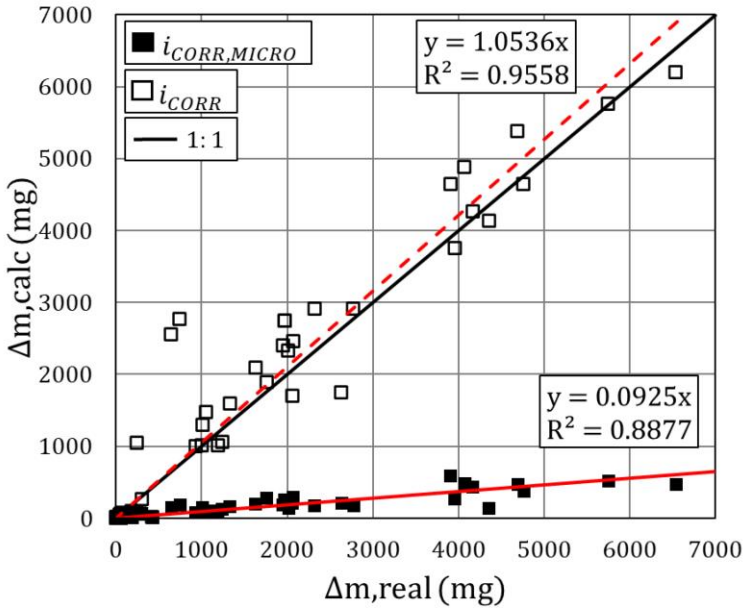

404

405 *Figure 16- Gravimetric comparison*

406 When only considering microcell processes, the theoretical values tended to underestimate
407 real mass loss due to corrosion by 90%. Conversely, when the analysis included macrocell
408 processes, a good fit appeared between the theoretical and real values, which deviated by 5%.
409 The big difference between both cases was caused by using a large cathodic surface because it
410 increased the importance of macrocell processes by recreating conditions that would take
411 place in densely reinforced areas. This fact demonstrates that monitoring rebars by measuring
412 only the $i_{CORR,MICRO}$ can lead to mistakes and uncertain estimations of structures' service life,
413 which would underestimate damage to zones affected by chlorides. Therefore, both microcell
414 and macrocell currents must be considered when designing embedded corrosion monitoring
415 systems to accurately control reinforced concrete structures located in marine environments.

416 ## ***5.- Conclusions***

417 The following conclusions can be drawn from this study on the influence that macrocell
418 currents have on monitoring reinforced concrete structures exposed to marine environments
419 for almost 1 year. This research was carried out using a large cathodic surface that simulates
420 the conditions that would take place in densely reinforced areas:

421 -the estimation done from Fick's second law of the time needed for chlorides to reach a rebar
422 and for corrosion onset provided good matches to reality;

423 -the existence of macrocell currents generates greater anodic polarisation in active rebar
424 zones, which favours chloride migration (negative electrical charge) towards the steel surface.
425 As a result of this, corrosion onset occurs earlier, the concentration of the chlorides around the
426 rebar is higher and the corrosion rate increases;

427 -when a rebar is not depassivated, steel mass loss is negligible due to macrocell currents.
428 However, upon corrosion onset, the influence of these currents is greater the worse concrete
429 quality is and the smaller the concrete cover is. In concrete C30, considering macrocell
430 currents, or not, leads to differences in the i_{CORR} values of almost two orders of magnitude,
431 and in concrete C50 of one order of magnitude. As a result of this, for concrete C30 and the 5
432 mm cover, mass loss was 50-fold higher than in the rebars not affected by macrocell currents;

-if, as is normally the case of many monitoring systems, the corrosion rate is determined only by measuring microcell currents (local corrosion), the obtained values tend to underestimate the real mass loss due to corrosion by, in this case, 90%. Conversely, when the analysis includes macrocell processes, a good match between theoretical and real values is obtained. Therefore, both microcell and macrocell currents must be considered when designing corrosion monitoring systems to accurately control reinforced concrete structures.

Acknowledgements

The authors thank the Spanish Government for Grant PID2020-119744RB-C21 funded by MCIN/AEI/10.13039/501100011033, and the support of the Universitat Politècnica de València. They are also grateful for the predoctoral scholarship granted to Josep Ramon Lliso Ferrando as part of the "Formación de Personal Investigador" programme from the Universitat Politècnica de València (FPI-UPV-2018), and Grant FPU 16/00723 funded by MCIN/AEI/ 10.13039/501100011033 and by "ESF Investing in your future".

Bibliography

AENOR. (2013). UNE-ISO 9297: Determinación de cloruros. Valoración de nitrato de plata con cromato como indicador (método de Mohr).

AENOR. (2019). UNE-EN 12390-11. Ensayos en Hormigón Endurecido. Parte 11 : Determinación de la resistencia a los cloruros del hormigón , difusión unidireccional.

Andrade, C., Alonso, C., Gulikers, J., Polder, R., Cigna, R., Vennesland, O., … Elsener, B. (2004). Recommendations of RILEM TC-154-EMC: "Electrochemical techniques for measuring metallic corrosion" Test methods for on-site corrosion rate measurement of steel reinforcement in concrete by means of the polarization resistance method. *Materials and Structures*, *37*(273), 623–643. https://doi.org/10.1617/13952

Andrade, C., Garcés, P., & Martínez, I. (2008). Galvanic currents and corrosion rates of reinforcements measured in cells simulating different pitting areas caused by chloride attack in sodium hydroxide. *Corrosion Science*, *50*(10), 2959–2964. https://doi.org/10.1016/j.corsci.2008.07.013

Andrade, C., Maribona, I. R., Feliu, S., González, J. A., & Feliu, S. (1992). The effect of macrocells between active and passive areas of steel reinforcements. *Corrosion Science*, *33*(2), 237–249. https://doi.org/https://doi.org/10.1016/0010-938X(92)90148-V

Andrade, C., & Martínez, I. (2005). Calibration by gravimetric losses of electrochemical corrosion rate measurement using modulated confinement of the current. *Materials and Structures/Materiaux et Constructions*, *38*(283), 833–841. https://doi.org/10.1617/14297

Andrade, Carmen. (2019). Propagation of reinforcement corrosion : principles , testing and modelling. *Materials and Structures*, *52*(1), 1–26. https://doi.org/10.1617/s11527-018-1301-1

Andrade, Carmen. (2020). Electrochemical methods for on-site corrosion detection. *Structural Concrete*, *21*(4), 1385–1395. https://doi.org/10.1002/suco.201900426

Angst, U., Elsener, B., Larsen, C. K., & Vennesland, Ø. (2009). Critical chloride content in reinforced concrete — A review. *Cement and Concrete Research*, *39*(12), 1122–1138. https://doi.org/10.1016/j.cemconres.2009.08.006

Angst, U. M. (2011). *Chloride induced reinforcement corrosion in concrete - Concept of critical chloride content – methods and mechanisms*. *Concept of Critical Chloride Content—*

Methods and …. Retrieved from http://www.diva-portal.org/smash/get/diva2:450383/FULLTEXT02

Angst, U. M. (2019). Predicting the time to corrosion initiation in reinforced concrete structures exposed to chlorides. *Cement and Concrete Research*, *115*(June 2018), 559–567. https://doi.org/10.1016/j.cemconres.2018.08.007

Bagheri, A., & Rastegar, M. M. (2019). Investigation of passive layer formation on steel rebars in foamed concrete. *Materials and Corrosion*, *70*(7), 1252–1261. https://doi.org/10.1002/maco.201810663

Balestra, C. E., Alessi Reichert, T., Savaris, G., Pansera, W. A., & A. Medeiros-Junior, R. (2020). Nondestructive Method for Estimation of Chloride Profiles: Correlation between Electrical Resistivity and Holliday-Empirical Equation. *Journal of Construction Engineering and Management*, *146*(10), 04020119. https://doi.org/10.1061/(asce)co.1943-7862.0001907

Balestra, C. E. T., Nakano, A. Y., Savaris, G., & Medeiros-Junior, R. A. (2019). Reinforcement corrosion risk of marine concrete structures evaluated through electrical resistivity: Proposal of parameters based on field structures. *Ocean Engineering*, *187*(February), 106167. https://doi.org/10.1016/j.oceaneng.2019.106167

Bentz, D. P., Jensen, O. M., Coats, A. M., & Glasser, F. P. (2000). Influence of silica fume on diffusivity in cement-based materials. I. Experimental and computer modeling studies on cement pastes. *Cement and Concrete Research*, *30*(6), 953–962. https://doi.org/10.1016/S0008-8846(00)00264-7

Bertolini, L., Pedeferri, P., Pastore, T., Bazzoni, B., & Lazzari, L. (1996). Macrocell Effects on Potential Measurements in Concrete Cathodic Protection Systems. *Corrosion*, *52*(7), 552–557. https://doi.org/https://doi.org/10.5006/1.3292145

Carnot, A., Frateur, I., Zanna, S., Tribollet, B., Dubois-Brugger, I., & Marcus, P. (2003). Corrosion mechanisms of steel concrete moulds in contact with a demoulding agent studied by EIS and XPS. *Corrosion Science*, *45*(11), 2513–2524. https://doi.org/10.1016/S0010-938X(03)00076-3

Chen, L., & Su, R. K. L. (2021). Corrosion rate measurement by using polarization resistance method for microcell and macrocell corrosion: Theoretical analysis and experimental work with simulated concrete pore solution. *Construction and Building Materials*, *267*, 121003. https://doi.org/10.1016/j.conbuildmat.2020.121003

Daniyal, M., & Akhtar, S. (2020). Corrosion assessment and control techniques for reinforced concrete structures: a review. *Journal of Building Pathology and Rehabilitation*, *5*(1), 1–20. https://doi.org/10.1007/s41024-019-0067-3

De Medeiros-Junior, R. A., De Lima, M. G., De Brito, P. C., & De Medeiros, M. H. F. (2015). Chloride penetration into concrete in an offshore platform-analysis of exposure conditions. *Ocean Engineering*, *103*, 78–87. https://doi.org/10.1016/j.oceaneng.2015.04.079

Dong, Z., & Poursaee, A. (2020). Corrosion behavior of coupled active and passive reinforcing steels in simulated concrete pore solution. *Construction and Building Materials*, *240*, 117955. https://doi.org/10.1016/j.conbuildmat.2019.117955

Dotto, J. M. R., De Abreu, A. G., Dal Molin, D. C. C., & Müller, I. L. (2004). Influence of silica fume addition on concretes physical properties and on corrosion behaviour of

520 reinforcement bars. *Cement and Concrete Composites*, *26*(1), 31–39.
521 https://doi.org/10.1016/S0958-9465(02)00120-8

522 Evans, U. R. (1978). *The Corrosion and Oxidation of Metals*. London, UK: Edward Arnold.
523 https://doi.org/https://doi.org/10.1002/maco.19780290130

524 Fernández, R. P., & Pardob, M. L. (2013). Offshore concrete structures. *Ocean Engineering*, *58*,
525 304–316. https://doi.org/10.1016/j.oceaneng.2012.11.007

526 Figueira, R. B. (2017). Electrochemical sensors for monitoring the corrosion conditions of
527 reinforced concrete structures: A review. *Applied Sciences (Switzerland)*, *7*(11).
528 https://doi.org/10.3390/app7111157

529 François, R. (2022). A discussion on the order of magnitude of corrosion current density in
530 reinforcements of concrete structures and its link with cross - section loss of
531 reinforcement, (2021), 158–168.

532 Gandía-Romero, J. M., Campos, I., Valcuende, M., Garciá-Breijo, E., Marcos, M. D., Payá, J., &
533 Soto, J. (2016). Potentiometric thick-film sensors for measuring the pH of concrete.
534 *Cement and Concrete Composites*, *68*, 66–76.
535 https://doi.org/10.1016/j.cemconcomp.2016.02.006

536 Gandía-Romero, José M., Bataller, R., Monzón, P., Campos, I., García-Breijo, E., Valcuende, M.,
537 & Soto, J. (2016). Characterization of embeddable potentiometric thick-film sensors for
538 monitoring chloride penetration in concrete. *Sensors and Actuators, B: Chemical*, *222*,
539 407–418. https://doi.org/10.1016/j.snb.2015.07.056

540 Gao, Y., Zheng, Y., Zhang, J., Wang, J., Zhou, X., & Zhang, Y. (2019). Randomness of critical
541 chloride concentration of reinforcement corrosion in reinforced concrete flexural
542 members in a tidal environment. *Ocean Engineering*, *172*(December 2018), 330–341.
543 https://doi.org/10.1016/j.oceaneng.2018.11.038

544 Hansson, C. M., Poursaee, A., & Laurent, A. (2006). Macrocell and microcell corrosion of steel
545 in ordinary Portland cement and high performance concretes. *Cement and Concrete*
546 *Composites*, *36*(6), 2098–2102. https://doi.org/10.1016/j.cemconres.2006.07.005

547 Karthick, S., Muralidharan, S., Lee, H. S., Kwon, S. J., & Saraswathy, V. (2019). Reliability and
548 long-term evaluation of GO-MnO 2 nano material as a newer corrosion monitoring sensor
549 for reinforced concrete structures. *Cement and Concrete Composites*, *100*(April 2017),
550 74–84. https://doi.org/10.1016/j.cemconcomp.2019.03.012

551 Karthick Subbiah, Saraswathy Velu, Kwon, S. J., Lee, H. S., Natarajan Rethinam, & Park, D. J.
552 (2018). A novel in-situ corrosion monitoring electrode for reinforced concrete structures.
553 *Electrochimica Acta*, *259*, 1129–1144. https://doi.org/10.1016/j.electacta.2017.10.088

554 Kupwade-Patil, K., Palkovic, S. D., Bumajdad, A., Soriano, C., & Büyüköztürk, O. (2018). Use of
555 silica fume and natural volcanic ash as a replacement to Portland cement: Micro and pore
556 structural investigation using NMR, XRD, FTIR and X-ray microtomography. *Construction*
557 *and Building Materials*, *158*, 574–590.
558 https://doi.org/10.1016/j.conbuildmat.2017.09.165

559 Liang, Y., & Wang, L. (2020). Prediction of corrosion-induced cracking of concrete cover: A
560 critical review for thick-walled cylinder models. *Ocean Engineering*, *213*(January),
561 107688. https://doi.org/10.1016/j.oceaneng.2020.107688

562 Lliso-Ferrando, J. R., Gasch, I., Martínez-Ibernón, A., & Valcuende, M. (2021). Macrocell
563 corrosion currents in simulated concrete pore solution and reinforced concrete. *In Press.*

564 Mansfeld, F. (1971). Area Relationships in Galvanic Corrosion. *Corrosion*, *27*(10), 436–442.
565 https://doi.org/https://doi.org/10.5006/0010-9312-27.10.436

566 Martínez-Ibernón, A., Lliso-Ferrando, J. R., Gandía-Romero, J. M., & Soto, J. (2021). Stainless
567 Steel Voltammetric Sensor to Monitor Variations in Oxygen and Humidity Availability in
568 Reinforcement Concrete Structures. *Sensors*.

569 Martínez-Ibernón, A., Ramón, J. E., Gandía-Romero, J. M., Gasch, I., Valcuende, M., Alcañiz, M.,
570 & Soto, J. (2019). Characterization of electrochemical systems using potential step
571 voltammetry. Part II: Modeling of reversible systems. *Electrochimica Acta*, *328*.
572 https://doi.org/10.1016/j.electacta.2019.135111

573 Martínez, I., & Andrade, C. (2009). Examples of reinforcement corrosion monitoring by
574 embedded sensors in concrete structures. *Cement and Concrete Composites*, *31*(8), 545–
575 554. https://doi.org/10.1016/j.cemconcomp.2009.05.007

576 Ministerio de Fomento. (2008). EHE-08. Instrucción de Hormigón Estructural. In *Ministerio de*
577 *Fomento. Normativa de edificación.* Ministerio de Fomento. Normativa de edificación.

578 Montemor, M. F., Simões, A. M. P., & Ferreira, M. G. S. (2003). Chloride-induced corrosion on
579 reinforcing steel: From the fundamentals to the monitoring techniques. *Cement and*
580 *Concrete Composites*, *25*(4-5 SPEC), 491–502. https://doi.org/10.1016/S0958-
581 9465(02)00089-6

582 Moradian, M., Shekarchi, M., Pargar, F., Bonakdar, A., & Valipour, M. (2012). Deterioration of
583 Concrete Caused by Complex Attack in Sewage Treatment Plant Environment. *Journal of*
584 *Performance of Constructed Facilities*, *26*(1), 124–134.
585 https://doi.org/10.1061/(asce)cf.1943-5509.0000189

586 NORDTEST; Nordic Cooperation. (1996). NT Build 208. Chloride content by Volhard titration.
587 *Nordtest Method*, *3*, 1–4.

588 Poursaee, A. (2016). *Corrosion of steel in concrete structures*. *Corrosion of Steel in Concrete*
589 *Structures*. Elsevier Ltd. https://doi.org/10.1016/B978-1-78242-381-2.00002-X

590 Pushpakumara, B. H. J., & Thusitha, G. A. (2021). Development of a Structural Health
591 Monitoring Tool for Underwater Concrete Structures. *Journal of Construction Engineering*
592 *and Management*, *147*(10), 04021135. https://doi.org/10.1061/(asce)co.1943-
593 7862.0002163

594 Qian, S., Zhang, J., & Qu, D. (2006). Theoretical and experimental study of microcell and
595 macrocell corrosion in patch repairs of concrete structures. *Cement and Concrete*
596 *Composites*, *28*, 685–695. https://doi.org/10.1016/j.cemconcomp.2006.05.010

597 Qiao, D., Nakamura, H., Yamamoto, Y., & Miura, T. (2016). Crack patterns of concrete with a
598 single rebar subjected to non-uniform and localized corrosion. *Construction and Building*
599 *Materials*, *116*, 366–377. https://doi.org/10.1016/j.conbuildmat.2016.04.149

600 Ramani, V., & Kuang, K. S. C. (2020). Monitoring chloride ingress in concrete using an imaging
601 probe sensor with sacrificial metal foil. *Automation in Construction*, *117*(May), 103260.
602 https://doi.org/10.1016/j.autcon.2020.103260

603 Ramón, J. E., Gandía-Romero, J. M., Bataller, R., Alcañiz, M., Valcuende, M., & Soto, J. (2020).
604 Potential step voltammetry: An approach to corrosion rate measurement of
605 reinforcements in concrete. *Cement and Concrete Composites*, *110*(4).
606 https://doi.org/10.1016/j.cemconcomp.2020.103590

607 Ramón, J. E., Martínez-Ibernón, A., Gandía-Romero, J. M., Fraile, R., Bataller, R., Alcañiz, M., …
608 Soto, J. (2019). Characterization of electrochemical systems using potential step
609 voltammetry. Part I: Modeling by means of equivalent circuits. *Electrochimica Acta*, *323*.
610 https://doi.org/10.1016/j.electacta.2019.134702

611 Ramón, José Enrique, Gandía-Romero, J. M., Valcuende, M., & Bataller, R. (2016). Integrated
612 sensor network for monitoring steel corrosion in concrete structures. *VITRUVIO -*
613 *International Journal of Architectural Technology and Sustainability*, *1*(1), 65.
614 https://doi.org/10.4995/vitruvio-ijats.2016.5191

615 Ramón, Jose Enrique, Martínez, I., Gandía-romero, J. M., & Soto, J. (2021). An embedded-
616 sensor approach for concrete resistivity measurement in on-site corrosion monitoring:
617 Cell constants determination. *Sensors*, *21*(7). https://doi.org/10.3390/s21072481

618 Revert, A. B., Hornbostel, K., De Weerdt, K., & Geiker, M. R. (2019). Macrocell corrosion in
619 carbonated Portland and Portland-fly ash concrete - Contribution and mechanism.
620 *Cement and Concrete Research*, *116*(October 2018), 273–283.
621 https://doi.org/10.1016/j.cemconres.2018.12.005

622 Rodrigues, R., Gaboreau, S., Gance, J., Ignatiadis, I., & Betelu, S. (2021). Reinforced concrete
623 structures: A review of corrosion mechanisms and advances in electrical methods for
624 corrosion monitoring. *Construction and Building Materials*, *269*, 121240.
625 https://doi.org/10.1016/j.conbuildmat.2020.121240

626 Rodríguez, P., Ramirez, E., Feliu, S., Gonzalez, J. A., & López, W. (1999). Significance of coplanar
627 macrocells to corrosion in concrete-embedded steel. *Corrosion*, *55*(3), 319–325.
628 https://doi.org/10.5006/1.3283994

629 Soleimani, S., Ghods, P., Isgor, O. B., & Zhang, J. (2010). Modeling the kinetics of corrosion in
630 concrete patch repairs and identification of governing parameters. *Cement and Concrete*
631 *Composites*, *32*(5), 360–368. https://doi.org/10.1016/j.cemconcomp.2010.02.001

632 Subramaniam, K. V, & Bi, M. (2010). Investigation of steel corrosion in cracked concrete :
633 Evaluation of macrocell and microcell rates using Tafel polarization response. *Corrosion*
634 *Science*, *52*(8), 2725–2735. https://doi.org/10.1016/j.corsci.2010.04.030

635 Torres-Acosta, A. A., & Castro-Borges, P. (2021). Durability control through design and health
636 monitoring during construction. *Structural Control and Health Monitoring*, *28*(2), 1–11.
637 https://doi.org/10.1002/stc.2670

638 Torres-Acosta, A. A., Patrón-Solares, A., & Alcántara-Lagunes, P. (2021). Durability health
639 monitoring during construction of concrete structures in marine environment. *Structural*
640 *Control and Health Monitoring*, *28*(3), 1–11. https://doi.org/10.1002/stc.2674

641 Valcuende, M., Lliso-Ferrando, J. R., Ramón-Zamora, J. E., & Soto, J. (2021a). Corrosion
642 Resistance of Ultra-High Performance Fibre-Reinforced Concrete. *Construction and*
643 *Building Materials*, *306*.
644 https://doi.org/https://doi.org/10.1016/j.conbuildmat.2021.124914

645 Valcuende, M., Lliso-Ferrando, J. R., Roig-Flores, M., & Gandía-Romero, J. M. (2021b). Porous
646 Structure of ultra-high-performance fibre-reinforced concretes. *Materials*, *14*(7).
647 https://doi.org/10.3390/ma14071637

648 Valipour, M., Shekarchi, M., & Ghods, P. (2014). Comparative studies of experimental and
649 numerical techniques in measurement of corrosion rate and time-to-corrosion-initiation
650 of rebar in concrete in marine environments. *Cement and Concrete Composites*, *48*, 98–

107. https://doi.org/10.1016/j.cemconcomp.2013.11.001

Vélez, W., Matta, F., & Ziehl, P. (2011). Acoustic emission monitoring of early corrosion in prestressed concrete piles. *Structural Control and Health Monitoring*, *22*, 873–887. https://doi.org/10.1002/stc.1723